Revealing the dynamic responses of Pb under shock loading based on DFT-accuracy machine learning potential

Enze Hou, 1,2 Xiaoyang Wang, 3 and Han Wang 3,4,*

¹Institute of Applied Physics and Computational Mathematics, Beijing 100094, China

²Graduate School of China Academy of Engineering Physics, Beijing 100088, China

³National Key Laboratory of Computational Physics,

Institute of Applied Physics and Computational Mathematics,

Fenghao East Road 2, Beijing 100094, China

⁴HEDPS, CAPT, College of Engineering and School of Physics,

Peking University, Beijing 100871, China

(Dated: November 18, 2025)

Lead (Pb) is a typical low-melting-point ductile metal and serves as an important model material in the study of dynamic responses. Under shock-wave loading, its dynamic mechanical behavior comprises two key phenomena: plastic deformation and shock induced phase transitions. The underlying mechanisms of these processes are still poorly understood. Revealing these mechanisms remains challenging for experimental approaches. Non-equilibrium molecular dynamics (NEMD) simulations are an alternative theoretical tool for studying dynamic responses, as they capture atomic-scale mechanisms such as defect evolution and deformation pathways. However, due to the limited accuracy of empirical interatomic potentials, the reliability of previous NEMD studies is questioned. Using our newly developed machine learning potential for Pb-Sn alloys, we revisited the microstructure evolution in response to shock loading under various shock orientations. The results reveal that shock loading along the [001] orientation of Pb exhibits a fast, reversible, and massive phase transition and stacking fault evolution. The behavior of Pb differs from previous studies by the absence of twinning during plastic deformation. Loading along the [011] orientation leads to slow, irreversible plastic deformation, and a localized FCC-BCC phase transition in the Pitsch orientation relationship. This study provides crucial theoretical insights into the dynamic mechanical response of Pb, offering a theoretical input for understanding the microstructure-performance relationship under extreme conditions.

I. INTRODUCTION

As a typical group IV metal, lead (Pb) has a low ambient-pressure melting point of approximately 600 K. Lead has a complex pressure-temperature phase diagram, Pb at ambient pressure has a ductile FCC phase and transforms to the HCP phase at ~13 GPa.^[1] At ~109 GPa, Pb transforms to the BCC phase. Both the FCC-HCP and HCP-BCC transitions are considered sluggish, weakly first-order transformations with minimal density changes.^[2] Under shock loading, the shock Hugoniot curve passes through all three phases, leading to complex dynamic behaviors, including plastic deformation^[3] and solid-state phase transitions^[4] at high strain rates. These unique properties make lead a key model material for studying materials response under dynamic loading.

Experimental studies of dynamic response of Pb have focused primarily on the macroscopic dynamic fracturing. For example, Chen et al.^[5] studied the mass and density distribution of fragmented Pb during its micro-spallation. Antipov et al.^[6] investigated the fragment of explosive shocked Pb and quantitatively determined ejecta, spallation, and undamaged regions. However, due to the lack of experimental approaches that characterize the micro-structures under extreme conditions, the atomistic-scale processes under the dynamic loading conditions, such as the defect evolution, phase transition, and void nucleation, remain poorly understood. Non-equilibrium

^{*} wang_han@iapcm.ac.cn

molecular dynamics (NEMD) simulations serve as a powerful alternative tool for investigating dynamic responses under shock loading. For example, Xiang et al.^[7–9] investigated shock-induced spallation of nano-crystal Pb, Wang et al.^[10], explored the spall response of release-melted lead. Mayer et al.^[11] simulated the sensitivity of spall strength to strain rates. These simulations complement and validate the experimental findings.

Importantly, NEMD simulations can resolve the microstructure evolution during the short period of dynamic loading prior to the dynamic fracture, which is critical to a comprehensive understanding of the microstructure-performance relationship under extreme conditions. For example, Li et al.^[12] studied the atomistic processes of shock-induced plasticity, which were found to be operative via the slipping and deformation twinning. They point out that twins formed due to the mutual impediments of the slip and cross-slips may act as nucleation sites for subsequent FCC-HCP phase transitions. In addition, BCC structures were observed to form along the Bain-Path, and mostly returned to FCC with further relaxation in tens of picoseconds.

It is worth noticing that most existing NEMD studies utilize empirical interatomic potential, a highly efficient formalism that employs fixed functional forms and a limited number of parameters fitted to several selected material properties. A well-known issue with empirical potentials is that they can hardly describe multiple phases accurately over a wide range of thermodynamic conditions. Meanwhile, their transferability is usually insufficient for accurately simulating a wide variety of defects. For instance, the study by Li et al. employed the embedded atom method (EAM) potential developed by Wang et al. [13] which accurately reproduces Pb's Hugoniot curve but underestimates the melting points above 40 GPa. Moreover, in our separate test of this EAM potential, the formation energy of the deformation twinning along the (111) plane is negative, which could possibly lead to the overestimation or unphysical formation of twins during MD simulations. The reliability of the simulation results could therefore be compromised by the lack of accuracies of the empirical potential. For Pb, first-principles calculations based on density functional theory (DFT) have been extensively applied to investigate its phase structures and phase diagram. For instance, Liu et al. and Cui et al. [14, 15] computed the critical pressures for phase transitions in Pb, with the calculated FCC-HCP and HCP-BCC transition pressures showing good agreement with experiments.^[1, 2] In addition, Cricchio et al.^[16] used ab initio molecular dynamics (AIMD) to determine the melting curve of Pb as a function of pressure, which also aligns well with experimental data. [17] Furthermore, Yu et al. [18] calculated the surface energy, which is consistent with experimental measurements.^[19] These agreements demonstrate the high reliability of DFT in predicting the properties of Pb. However, AIMD cannot be directly applied to simulate dynamic mechanical responses, as the computational complexity of DFT scales cubically with the number of electrons, making such simulations prohibitively expensive for large systems and long timescales.

Fortunately, recent development of the machine-learning potential (MLP)^[20-32] has revolutionized atomic scale simulations by offering both high accuracy and computational efficiency in research fields such as perovskites ^[33], nuclear materials ^[34], superconductors ^[35], high-energy-density materials ^[36], high pressure water phases ^[37, 38] and atmosphere of gas giant planets ^[39]. MLPs have also been widely employed in non-equilibrium dynamic simulations. For instance, Gao et al.^[40] investigated the ultrafast laser-induced melting of copper nanofilms using an MLP; Zeng et al.^[41] examined liquid iron under extreme conditions; Liu et al.^[42] studied the spallation behavior of p-phenylene terephthalamide crystals; D'Souza et al.^[43] explored the behavior of deuterium under shock loading; Pan et al.^[44] analyzed shock compression pathways in pyrite silica; and Zeng et al.^[45] researched the shock-induced phase transition of solid iron at high pressures. These examples collectively demonstrate the applicability and reliability of MLPs in simulating the dynamic responses of materials.

We recently developed a machine-learned potential (MLP) named DP-PbSn, $^{[46]}$ tailored for Pb-Sn alloy with up to 30 at.% Sn. With the aid of the non-von Neumann molecular dynamics

(NVNMD) architecture,^[47] this potential is able to access large-scale NEMD simulations including millions of atoms with first-principles accuracy over a wide thermodynamic range (0–5000 K, 0–100 GPa). In this work, we employ this potential in NEMD simulations to revisit the atomistic processes in Pb's dynamic response, including the shock induced plasticity and the evolution of the BCC phase during shock loading. Meanwhile, the anisotropy of shock-induced plastic deformation and phase transformation of Pb is investigated.

The findings in this study may provide new mechanistic insights into the dynamic mechanical response of Pb. Meanwhile, the techniques used in this study can be applied to investigating the dynamic processes of other materials.

II. METHODS

In this section, we first briefly introduce the MLP, then present the molecular dynamics setups employed in this study.

A. The MLP: DP-PbSn

The MLP employed in this study, namely DP-PbSn, was developed based on the DeepMD-Kit^[28, 48] framework. This potential was trained on a dataset comprising over 8217 configurations, covering a thermodynamic range of 0–100 GPa and 0–5000 K. The dataset encompassed molecular dynamics trajectories of BCC, FCC, HCP, and liquid phases of Pb-Sn alloy, sampled both during the evolution toward equilibrium and after the equilibrium under the target thermodynamic conditions. These phases are experienced by the material along the shock Hugoniot during compression. Moreover, the structures of mono-vacancy and free surfaces were included in the training dataset, which enhances the reliability of the potential in describing fracture nucleation. For dataset generation, the DFT calculations utilized a plane-wave basis set implemented in the ABACUS code. The Perdew-Burke-Ernzerhof (PBE) exchange-correlation functional within the generalized gradient approximation (GGA) was used. An energy cutoff of 100 Ry and a Monkhorst-Pack k-point sampling grid spacing of 0.15 Å⁻¹ were selected. The Optimized Norm-Conserving Vanderbilt (ONCV) pseudopotentials from PseudoDojo $5^{[53, 54]}$ were employed.

The MLP achieved a testing RMSE on an independent test set of 2.27 meV/atom, 40.6 meV/Å, and 25.8 meV/atom for energy, force, and virial tensor, respectively. The detailed DP-PbSn characterization results are presented in Ref.[46]

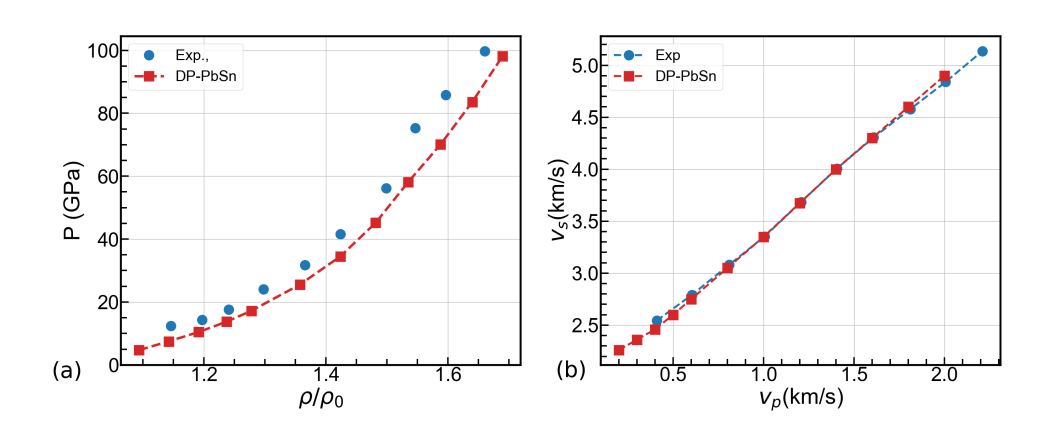


Fig. 1. The Hugoniot curve predicted by DP-PbSn. (a) the pressure-density relationship compared with the experimental result from Ref.[55]. (b) The shockwave velocity-piston velocity relationship compared with the experimental results.^[55] These results were reproduced from Ref.[46] with the permission of the authors.

The Hugoniot curve of Pb calculated using NEMD simulations is presented in Fig. 1. While the pressure-density (P- ρ) relationship along the Hugoniot predicted by DP-PbSn followed the general trend of the experimental data (Fig. 1 (a)), it exhibited a nearly constant shift towards a lower pressure. The observed deviation between the calculated Hugoniot curve and experimental data likely stems from systematic errors in DFT calculations when compared to experimental results. As evidenced by the equation of state reported in Ref.[10], DFT calculations may consistently underestimate the pressure relative to experimental measurements at equivalent volumes. This systematic underestimation aligned with the discrepancies shown in our results. The particle velocity-wave velocity ($v_{\rm p}-v_{\rm s}$) relationship obtained with DP-PbSn is shown in Fig. 1 (b), demonstrating near-linear behavior that closely matched the experimental measurements.^[55] These Hugoniot curve results further validate the applicability of DP-PbSn for investigating dynamic mechanical responses.

B. Molecular Dynamics Setup

We performed NEMD simulations on FCC-Pb samples with dimensions of approximately 100 Å \times 100 Å \times 1,000 Å along the x, y, and z axes. The samples comprised 320,000 atoms. The simulation cell size was sufficient to capture the dynamic processes from shock compression to the onset of dynamic fracture, while also representing a practical compromise given the substantial computational cost associated with the MLP. Prior to dynamic loading, the sample was equilibrated at 300 K and zero pressure with the NPT ensemble for 50 ps. Periodic boundary conditions were applied along all dimensions during the equilibrium simulation.

In the non-equilibrium simulation, dynamic loading was applied via a piston at the lower z boundary of the sample, with a controlled particle velocity vp ranging from 0.2 to 1.4 km/s, generating a compressive shock wave that propagated toward the upper z boundary.^[56] An NVE ensemble was applied to the system throughout the NEMD simulations. Periodic boundary conditions were maintained in the x and y dimensions, while the boundary condition along the z dimension was set to free. The piston was removed immediately when the shock wave reached the upper z-boundary. As a result, a release wave from the lower z-boundary and a rarefaction wave reflected from the upper z-boundary were initiated simultaneously. During the NEMD simulations, we implemented an adaptive time step ranging from 0.001 fs to 1 fs, ensuring the maximum atomic displacement within any single time step did not exceed 0.1 Å. The use of an adaptive time step effectively balanced the temporal resolution required to capture rapidly evolving dynamical processes against the computational cost associated with MLPs.

The equilibrium and NEMD simulations were implemented using the LAMMPS package.^[57] The material properties were evaluated by analyzing thin slices along the z-direction of the system. The width of each slice was 2.0 Å. Within each slice, we computed the per-atom velocity (v_i) , pressure, shear stress, and local temperature. The shear stress was calculated as:

$$\tau = \frac{1}{2}(\sigma_{zz} - \frac{1}{2}(\sigma_{xx} + \sigma_{yy})), \tag{1}$$

where σ is the stress tensor for each atom. The local temperature was calculated as:

$$T = \frac{1}{3Nk_{\rm b}} \sum_{i=1}^{N} m_i \left(v_{i,x}^2 + v_{i,y}^2 + (v_{i,z} - v_{\rm com,z})^2 \right), \tag{2}$$

where $v_{\text{com,z}}$ is the velocity of the center of mass of each slice along the z-direction, which was properly reduced for temperature evaluation.

The crystal structure in the NEMD snapshots was primarily determined via the polyhedral template matching (PTM) analysis.^[58] The visualization of the snapshots was performed using the OVITO software.^[59]

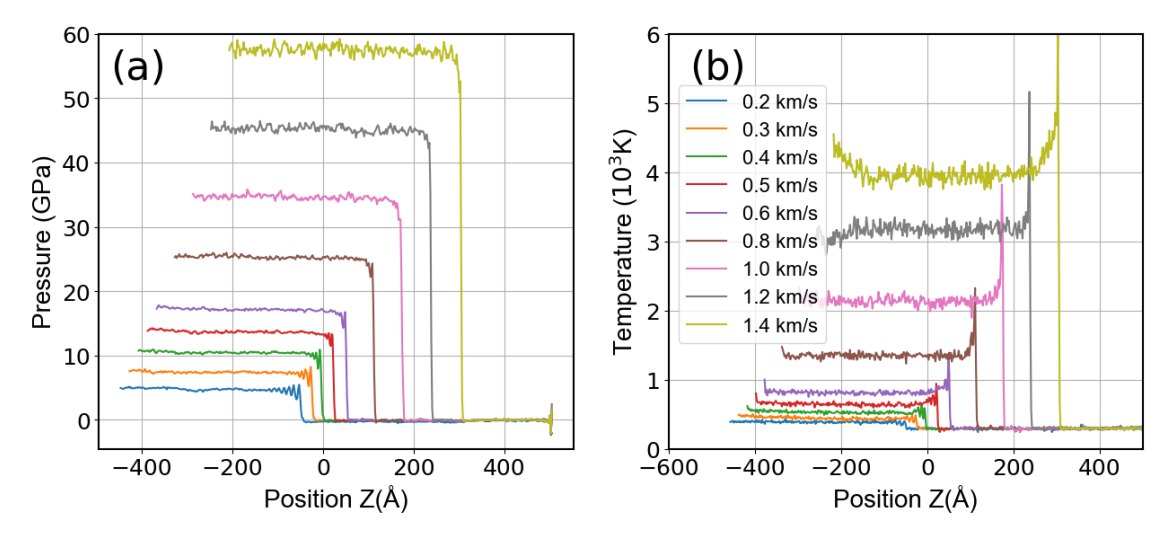


Fig. 2. The spatial distributions of thermodynamic quantities during loading along the [001] direction at 20 ps after piston loading. (a) Pressure distribution. (b) Local temperature distribution.

III. RESULTS

A. Shock along [001] direction

Figs. 2 (a) and (b) present the spatial distributions of pressure and temperature along the z-direction at a representative simulation time after shock loading along the [001] direction. For all simulated v_p values, the compressed region exhibited a relatively uniform pressure plateau behind the shock wave front. The temperature profiles showed peak values at the shock wave front, and gradually converged to plateau. The maximum (P,T) condition in our simulations was (58 GPa, 4000 K), which lay within the thermodynamic range covered by DP-PbSn.

Fig. 3 presents the distribution of shear stress and the corresponding snapshots during shock loading. The shear stress profiles effectively revealed the microstructure evolution under compression. At $v_{\rm p}=0.2$ km/s, Pb underwent neither plastic deformation nor solid-phase transformation, maintaining an FCC structure that exhibited characteristically high shear stress. With increasing $v_{\rm p}$, the shear stress within the compressed region was significant relaxed, accompanied by plastic behavior. A notable phenomenon emerged where atoms near the shock front were transiently identified as BCC structure. However, these metastable BCC structures rapidly degenerated into deformed FCC phases within a few picoseconds. Stripe-like region identified as HCP structure emerged along 45° to the shock propagation direction, corresponding to stacking faults within the FCC phase. This transient BCC formation and subsequent reversion behavior has been previously reported by Li et al. [12]

The major difference between the results of this study and those of Li et al. [12] was the activated deformation mechanisms in shock induced plasticity. In this study, only slipping was activated during [001] loading. However, in the study by Li et al., not only slipping but also twinning was operative during plastic deformation, which was possibly caused by the unphysical negative twin formation energy (-0.51 meV/ $\mathring{\rm A}^2$) predicted by the EAM potential. By contrast, DP-PbSn

predicted nearly $1.0~{\rm meV/\mathring{A}^2}$ formation energy of the twin, which was an underestimation of the DFT value $3.3~{\rm meV/\mathring{A}^2}$. Twinning structure was not included in the dataset of DP-PbSn. However, even with this underestimation, the twinning was still not operative during the shock compression in our simulation.

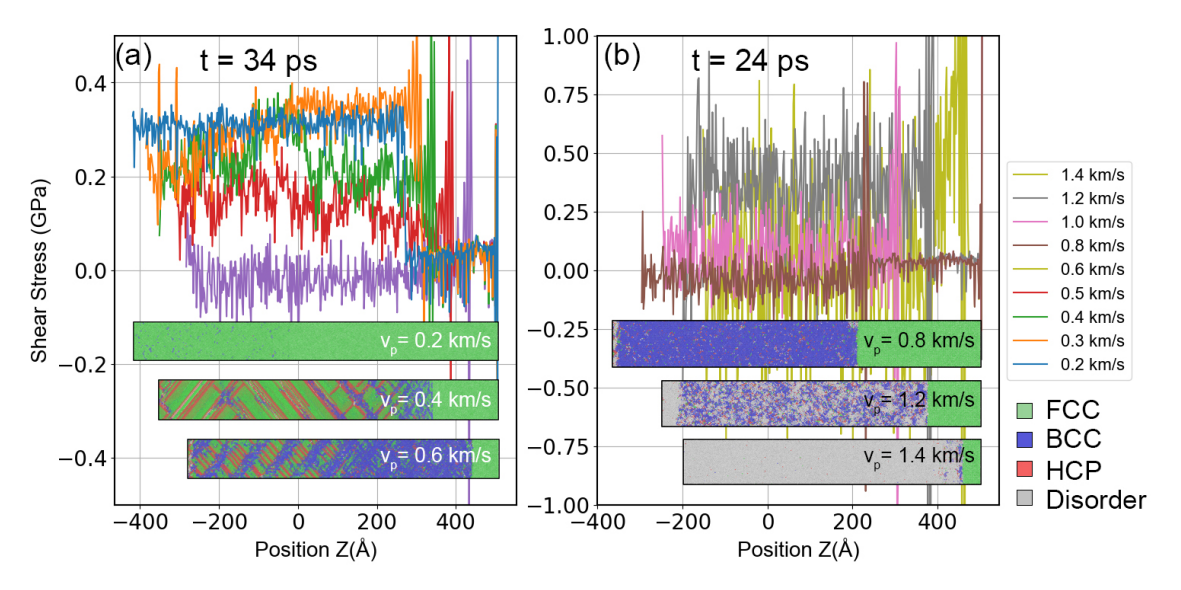


Fig. 3. The distribution of shear stress and the representative snapshots during loading along the [001] direction . (a) $0.2 \text{ km/s} \le v_p \le 0.6 \text{ km/s}$ at 34 ps after piston loading. (b) $0.8 \text{ km/s} \le v_p \le 1.4 \text{ km/s}$ at 24 ps after piston loading.

Further increasing $v_{\rm p}$ drove the P-T condition in the compressed region closer to the BCC phase region on the equilibrium phase diagram. Consequently, the stability of shock-induced BCC structures was enhanced. At $v_{\rm p}=0.6$ km/s, the proportion of BCC regions within the shock wave exceeded that of deformed FCC phase, accompanied by near-zero shear stress in the compressed material. When $v_{\rm p}$ was further increased to 0.8 km/s, nearly all atoms within the compressed regions were identified BCC structures. The reversion to FCC structures completely disappeared. The shear stress distribution remained approximately zero, demonstrating that both the FCC-BCC phase transformation and plastic deformation under shock loading effectively relaxed the shear stress.

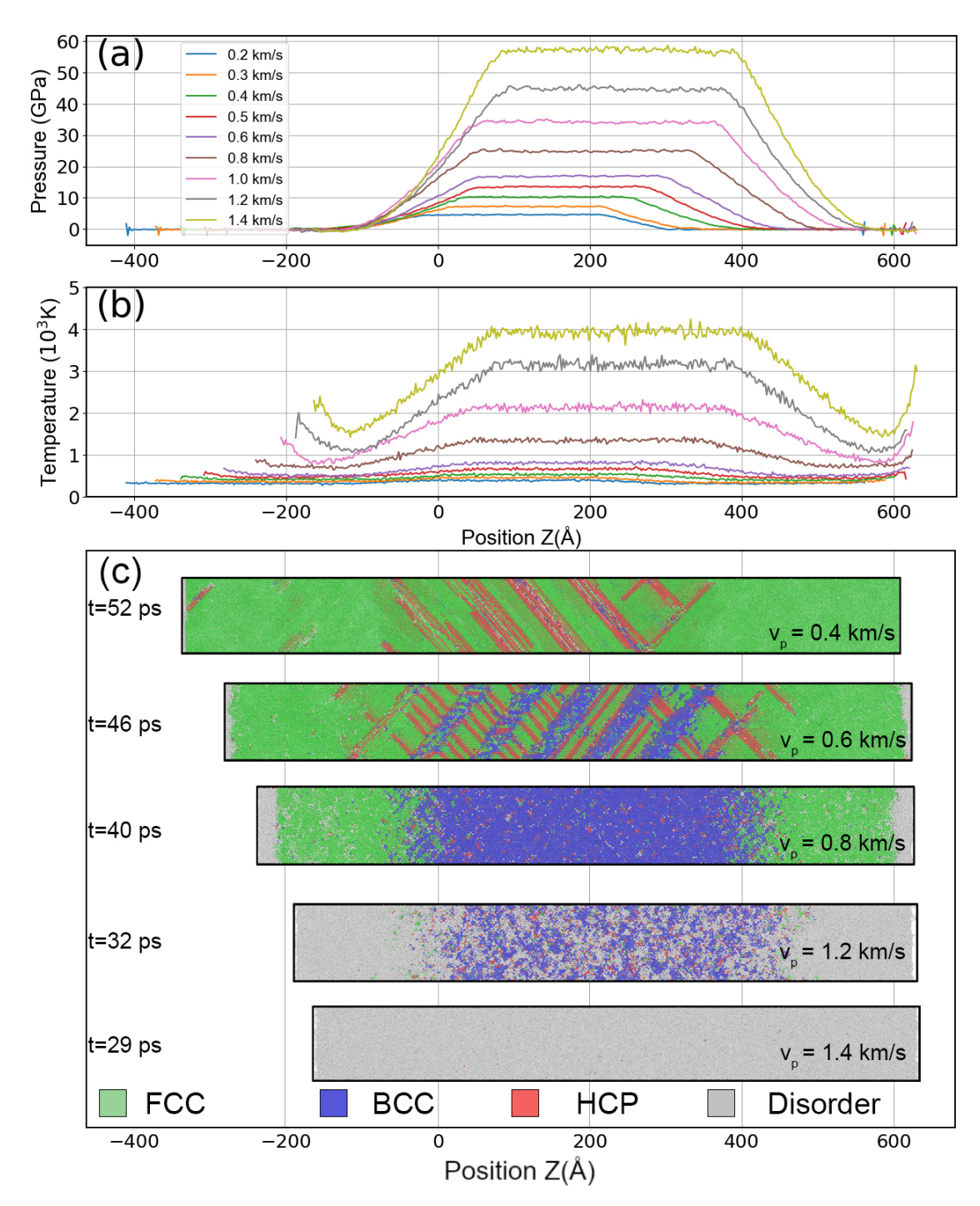


Fig. 4. (a) The distribution of pressure during [001] unloading. (b) The distribution of temperature during [001] unloading. (c) Snapshots at representative simulation times after piston loading.

Interestingly, while the compressed region at $v_{\rm p}=0.8$ km/s became predominantly BCC-structured, the corresponding thermodynamic conditions did not actually enter the equilibrium BCC phase region. This apparent contradiction stemmed from the unique FCC-BCC transition pathway under shock loading along the [001] direction. The Bain-path^[60] for the FCC-BCC transformation required substantial compression along the [001] direction, which experienced a tremendously high energy barrier for the near-equilibrium processes. However, in dynamic processes, shock compression along the [001] orientation drove FCC deformation that aligned with the Bain

path, enabling a forced transformation from FCC to BCC within picoseconds. Once formed, BCC phase was maintained if it was dynamically stable in the reached (P,T) condition, or reverted to the deformed FCC structure if the (P,T) was too low.

Further increasing v_p led to a gradually diminished shock-induced BCC phase. As shown in Fig. 3 (b), at $v_p = 1.2$ km/s, atoms in the compressed regions became increasingly disordered. When v_p reached 1.4 km/s, almost all atoms within the shock front became disordered. The corresponding thermodynamic condition (58 GPa, 4000 K, as shown in Fig. 2) exceeded the melting line in the equilibrium phase diagram^[4], indicating the shock-induced melting.

The above processes showed a typical phase transformation from FCC to BCC and shock-induced melting. No FCC to HCP phase transformation was observed. It is well established that this phase transformation is sluggish even at experimental timescales. Therefore, we considered that within the short timescales accessible in NEMD simulations, substantial nucleation of the HCP phase was unlikely to be observed. Moreover, the FCC-to-HCP phase transformation is known to be accomplished by the sequential glide of Shockley partial dislocations on every other close-packed {111} plane in the FCC lattice. This mechanism requires a higher dislocation density than that observed in our simulation results, which explains the absence of nucleation in our study. This discrepancy was likely attributable to the use of a perfect single crystal in the molecular dynamics simulation. In real materials, the presence of defects across various scales can act as dislocation sources under rapid deformation, potentially generating a higher density of dislocations and thus initiating HCP nucleation.

Upon reaching the free surface, the shock wave generated a rarefaction wave that propagating in the opposite direction. At the same time, the piston was unloaded, leading to the creation of a release wave. Fig. 4 illustrates the distribution of pressure and temperature alongside with the typical snapshots during the unloading process. Following the rarefaction wave and the release wave, temperature and pressure in the unloaded region gradually decreased. At $v_{\rm p} \leq 0.8$ km/s, the unloaded region predominantly retained an FCC structure. Stacking faults and the BCC phase in most of the unloaded region disappeared. The reversion from BCC to FCC during unloading followed the reverse Bain path, wherein the BCC lattice underwent significant uniaxial tensile deformation along its [001] direction to form the FCC phase. At $v_{\rm p} \geq 1.0$ km/s, the unloaded region exhibited a disordered phase rather than the FCC phase, demonstrating characteristic features of release melting.

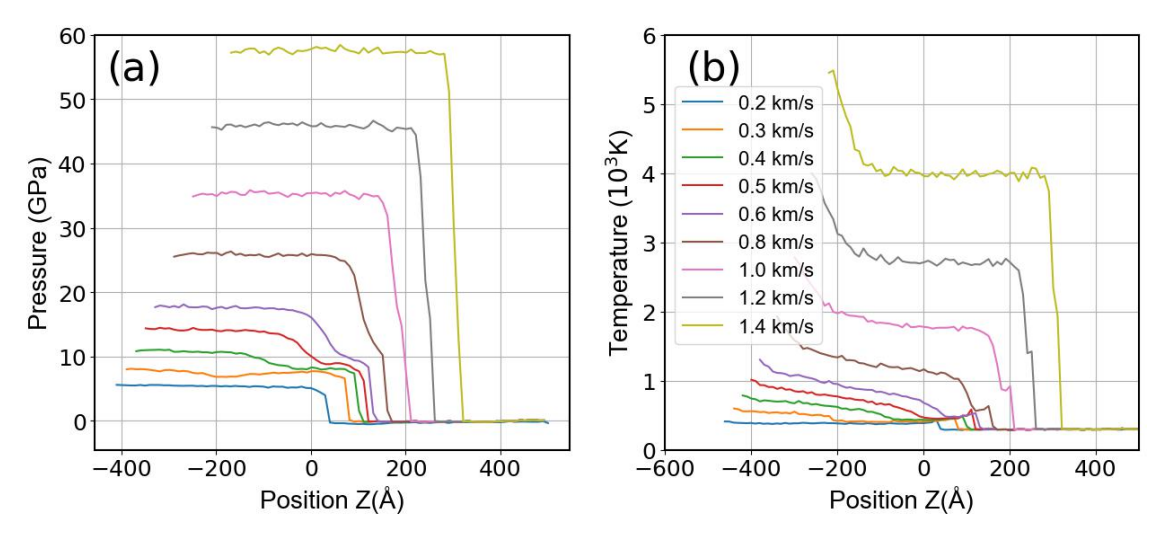


Fig. 5. The spatial distributions of thermodynamic quantities during loading along the [011] direction at 20 ps after piston loading. (a) Pressure distribution. (b) Local temperature distribution.

B. Shock along [011] direction

Shock loading along the [001] direction induces an FCC-BCC transition with deformation consistent with the Bain path. When this consistency is not satisfied, FCC-BCC transition behavior is expected to be different. Moreover, when loading along other orientations, the activated slip plane may not lie perfectly 45° to the shock propagation direction, where the shear stress is maximum. Thus, anisotropy in Pb's shock-induced plasticity and phase transition is expected. To further investigate this anisotropy, additional simulations were conducted with the piston loading along the [011] orientation.

Fig. 5 shows the pressure and temperature distributions during shock loading along the [011] direction. Compared with the loading along the [001] orientation, the compressed region along the [011] loading exhibits a more complex thermodynamic state evolution.

In the velocity range of 0.3 km/s $\leq v_{\rm p} \leq$ 1.0 km/s, the pressure in the compressed region underwent a relaxation period before reaching its plateau value. In comparison to the [001] loading cases, these relaxations were significantly slower. The temperature within the compressed region exhibited a distinct gradient, indicating that the compressed material did not immediately achieve a Hugoniot equilibrium state upon compression, but underwent complex evolution. At $v_{\rm p} \geq$ 1.2 km/s, the evolution of (P,T) distribution reproduced its behavior under the [001] loading case. The pressure and temperature reached their plateaus immediately after the compression.

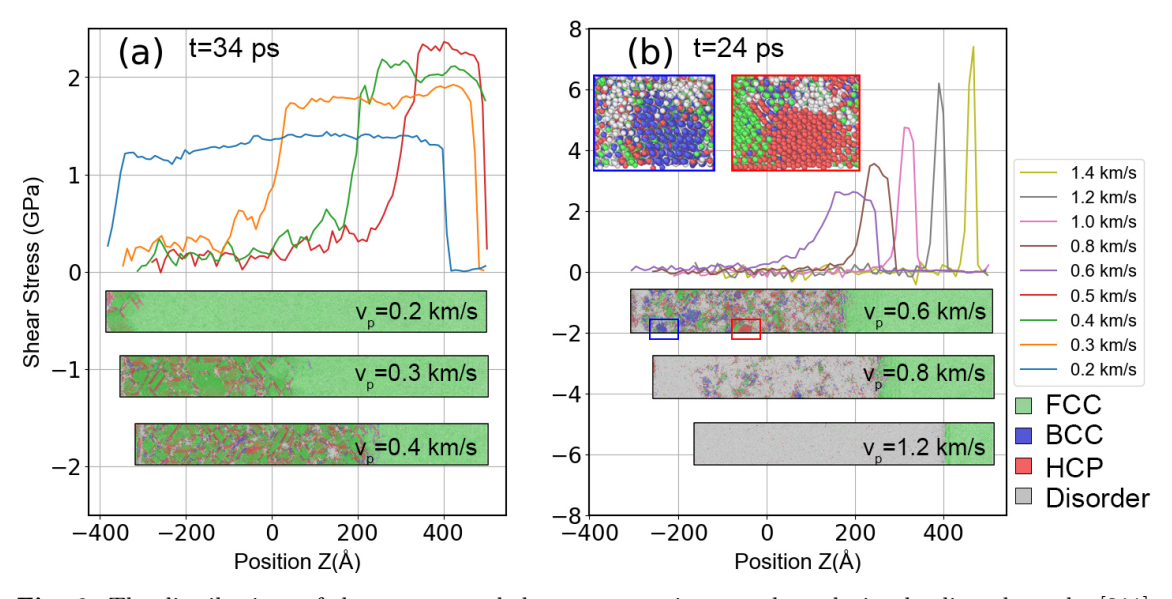


Fig. 6. The distributions of shear stress and the representative snapshots during loading along the [011] direction at 20 ps after piston loading. (a) $0.2 \text{ km/s} \le v_p \le 0.4 \text{ km/s}$ at 34 ps after piston loading. (b) $0.6 \text{ km/s} \le v_p \le 1.4 \text{ km/s}$ at 24 ps after piston loading. The blue and red rectangles mark the regions where the bulk BCC and HCP phases are formed.

The shear stress distributions as well as the representative snapshots of NEMD simulations in the [011] loading cases at various v_p are shown in Fig. 6. At 0.2 km/s $\leq v_p \leq$ 0.4 km/s (Fig. 6 (a)), stacking fault structures emerged along 60° orientations to the shock wave propagation direction. When v_p was further increased to 0.6 km/s(Fig. 6 (b)), the stacking fault structure became less prevalent, instead, bulk HCP-phase (the red rectangles in Fig. 6 (b)) domains as well as the bulk BCC-phase (the blue rectangles in Fig. 6 (b)) appeared in the compressed region. Meanwhile, the proportion of disordered structures showed a marked increase. With a further increase in v_p , the proportion of disordered structures within the shock wave continued to increase. When $v_p \geq 1.2$ km/s, the compressed region became almost entirely disordered. Meanwhile, the shear

stress became nearly zero in the compressed region, showing clear signatures of shock induced melting.

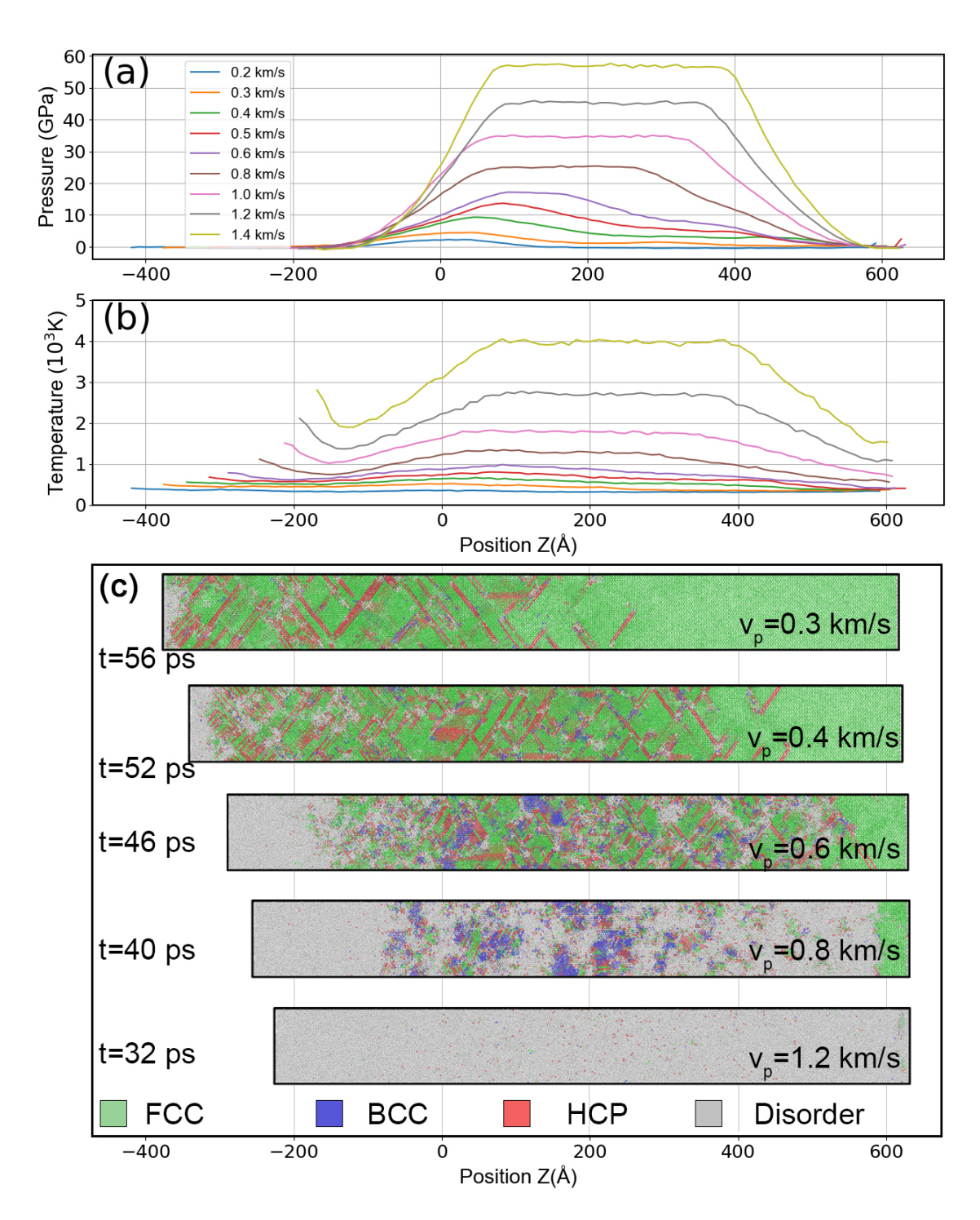


Fig. 7. (a) Pressure distribution during [011] unloading. (b) Temperature distribution during [001] unloading. (c) Snapshots at representative simulation times after piston loading.

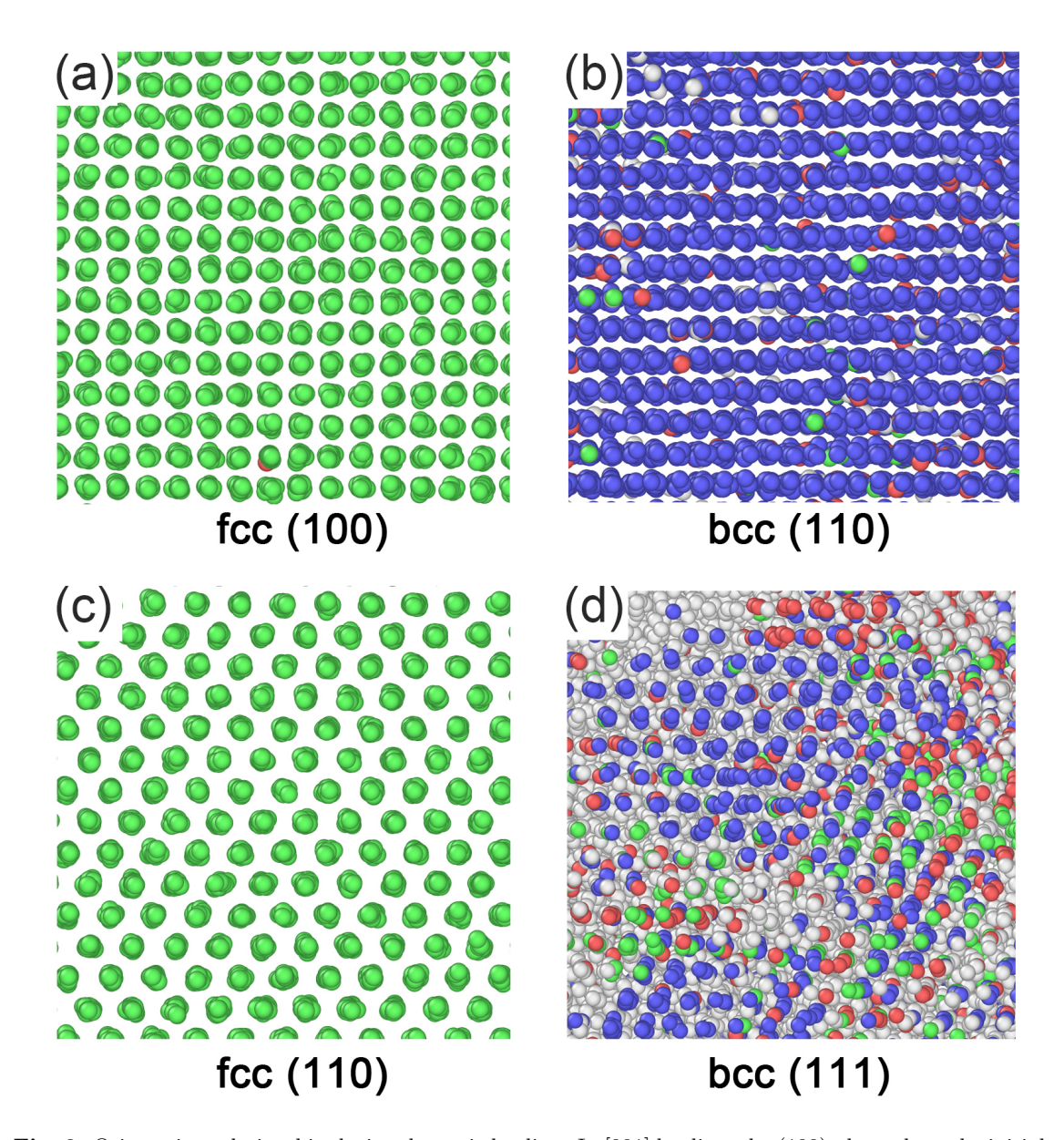


Fig. 8. Orientation relationship during dynamic loading. In [001] loading, the (100) plane along the initial FCC phase shown in (a) is aligned along with the (110) plane in the BCC phase in the compressed region shown in (b). In [011] loading, the (110) plane along the initial FCC phase shown in (c) is aligned along with the (111) plane in the BCC phase in the compressed region shown in (d).

The pressure and temperature distributions, together with representative snapshots during the unloading along the [011] direction are shown in Fig. 7. Pb exhibits significantly different behavior in [011] unloading compared to the [001] unloading. The key difference lies in the distribution of stacking faults. As shown in Figs. 7 (a) and (b), while the temperature and pressure gradually decay in the released region, the stacking faults generated during loading stage were not instantly eliminated upon unloading. For example, as shown in Fig. 7 (c), the unloaded region at $v_{\rm p} = 0.3, 0.4$ and 0.6 km/s retains a substantial density of such plastic deformation defects identified as layered HCP structures, though the corresponding pressure had already decayed to zero. At $v_{\rm p} \geq 0.8$ km/s atoms in the unloaded region were identified as the disordered structure, showing significant characteristics of release melting.

The anisotropy of plastic deformation can be explained by the variations of Schmidt factor of activated slip systems. In [001] loading the activated slip systems are [011]/(1-11) and $[0\bar{1}1]/(111)$.

Under the uniaxial compression and tension, these slip systems exhibit the maximum Schmidt factor 0.5. This indicates that this slip system can be subjected to the maximum resolved shear stress from the applied stress, which facilitates the activation of the slip systems. However, in [011] loading, the two primarily activated slip systems are [110]/(1-11) and $[\bar{1}10]/(111)$. The Schmidt factor of these slip systems are 0.433, which causes a reduction of the resolved shear stresses on these slip systems.

The anisotropy of shock-induced FCC-BCC phase transformation manifests not only in the proportion of phase transition region, but also in the crystallographic orientation relationships. The FCC and BCC phases in the region under the [001] shock loading are shown in Figs. 8 (a) and (b), respectively, exhibiting the orientation relationship: $[001]_{FCC}||[001]_{BCC}$; $[100]_{FCC}||[110]_{BCC}$. This orientation relationship is typical of the well-known Bain-Path. However, as shown in Figs. 8 (c) and (d), the FCC and BCC phases under [011] loading exhibit a distinct orientation relationship approximated by $[110]_{FCC}||[111]_{BCC}$ and $[100]_{FCC}||[110]_{BCC}$, which is in agreement with the orientation relationship discovered by Pitsch. Nevertheless, the NEMD simulations do not provide further insight into the detailed transformation pathways of these processes.

IV. CONCLUSION

To elucidate the atomistic scale processes governing the microstructure evolution of Pb in response to shock loading, we employed a high-accuracy MLP for Pb-Sn alloys to investigate shock-induced plasticity, phase transformations, melting, and defect evolution during loading-unloading processes under shock impact along both [001] and [011] directions. The principal findings are as follows:

- 1. Shock plasticity exhibits pronounced anisotropy. Under [001] loading, rapid stacking fault formation occurs, which is subsequently eliminated during unloading. In contrast, [011] loading generates stacking faults more slowly, yet most of these defects persist upon unloading. This anisotropy arises from the significantly larger Schmidt factors on operative slip systems during [001] loading.
- 2. FCC-BCC phase transformation during shock loading also exhibits strong anisotropy. Under [001] loading, the transformation follows the Bain path and reverts to the FCC phase during unloading. In contrast, [011] directional loading leads to the FCC-BCC phase transition following the Pitsch orientation relationship.

The findings presented in this study establish a crucial theoretical foundation for subsequent dynamic experiments investigating lead's shock-induced phase behavior. The techniques used in this study can be applied to the study of the dynamic processes of other materials of interest in this field, such as Al, Cu and Fe. Our future work will systematically investigate the transformation pathway and underlying mechanisms associated with this unique orientation relationship.

ACKNOWLEDGMENT

The work was supported by the National Key R & D Program of China under Grant No. 2022YFA1004300, and the National Natural Science Foundation of China under Grant No. 12404004.

- [2] Kuznetsov A, Dmitriev V, Dubrovinsky L, Prakapenka V and Weber H P 2002 Solid State Commun. **122** 125
- [3] Sharma S M, Turneaure S J, Winey J M and Gupta Y M 2020 Phys. Rev. Lett. 124 235701
- [4] Krygier A, Powell P D, McNaney J M, Huntington C M, Prisbrey S T, Remington B A, Rudd R E, Swift D C, Wehrenberg C E, Arsenlis A, Park H S, Graham P, Gumbrell E, Hill M P, Comley A J and Rothman S D 2019 *Phys. Rev. Lett.* **123** 205701
- [5] Chen Y, Ren G, Tang T, Li Q and Hu H 2016 Shock Waves 26 221
- [6] Antipov M V, Arinin V A, Georgievskaya A B, Gnutov I S, Zamyslov D N, Kalashnikov D A, Lebedeva M O, Lebedev A I, Mikhailov A L, Ogorodnikov V A, Panov K N, Pupkov A S, Rayevskiy V A, Sokolova A S, Syrunin M A, Tkachenko B I, Utenkov A A, Fedorov A V, Finyshin S A, Chudakov E A and Yurtov I V 2017 J. Dyn. Behav. Mater. 3 300
- [7] Xiang M, Hu H and Chen J 2013 J. Appl. Phys. 113 144312
- [8] Xiang M, Hu H and Chen J 2013 Key Eng. Mater. 577-578 613
- [9] Xiang M, Hu H, Chen J and Long Y 2013 Model. Simul. Mater. Sci. Eng. 21 055005
- [10] Wang K, Zhang F, He A and Wang P 2019 J. Appl. Phys. 125 155107
- [11] Mayer A E and Mayer P N 2020 Int. J. Fract. 222 171
- [12] Li G, Wang Y, Wang K, Xiang M and Chen J 2019 J. Appl. Phys. 126 075902
- [13] Wang K, Zhu W, Xiang M, Xu Y, Li G and Chen J 2018 Model. Simul. Mater. Sci. Eng. 27 015001
- [14] Liu A Y, Garca A, Cohen M L, Godwal B K and Jeanloz R 1991 Phys. Rev. B 43 1795
- [15] Cui S, Cai L, Feng W, Hu H, Wang C and Wang Y 2008 Phys Status Solidi B 245 53
- [16] Cricchio F, Belonoshko A B, Burakovsky L, Preston D L and Ahuja R 2006 Phys. Rev. B 73 140103
- [17] Vohra Y K and Ruoff A L 1990 Phys. Rev. B 42 8651
- [18] Yu D and Scheffler M 2004 Phys. Rev. B 70 155417
- [19] Bombis C, Emundts A, Nowicki M and Bonzel H 2002 Surf. Sci. 511 83
- [20] Thompson A P, Swiler L P, Trott C R, Foiles S M and Tucker G J 2015 J. Comput. Phys. 285 316
- [21] Shapeev A V 2016 MULTISCALE MODEL SIM 14 1153
- [22] Behler J and Parrinello M 2007 Phys. Rev. Lett. 98 146401
- [23] Bartók A P, Payne M C, Kondor R and Csányi G 2010 Phys. Rev. Lett. 104 136403
- [24] Chmiela S, Tkatchenko A, Sauceda H E, Poltavsky I, Schütt K T and Müller K R 2017 Sci. Adv. 3 e1603015
- [25] Schütt K, Kindermans P J, Sauceda H E, Chmiela S, Tkatchenko A and Müller K R 2017 Advances in Neural Information Processing Systems 30, December 4–9, 2017, Long Beach, CA, USA p 992
- [26] Smith J S, Isayev O and Roitberg A E 2017 Chem. Sci. 8 3192
- [27] Han J, Zhang L, Car R and E W 2018 Commun. Comput. Phys. 23 629
- [28] Zhang L, Han J, Wang H, Saidi W A, Car R and E W 2018 Advances in Neural Information Processing Systems 31 (NeurIPS 2018), December 3–8, 2018, Montréal, Canada
- [29] Wood M A and Thompson A P 2017 arXiv:1702.07042 [physics.comp-ph]
- [30] Kostiuchenko T S, Shapeev A V and Novikov I S 2024 Chin. Phys. Lett. 41 066101
- [31] Zhao K J and Song Z G 2025 Chin. Phys. B **34** 066101
- [32] Xiong J H, Qi Z J, Liang K, Sun X, Sun Z P, Wang Q J, Chen L W, Wu G and Shen W 2023 Chin. Phys. B 32 128101
- [33] Yang F, Zeng Q, Chen B, Kang D, Zhang S, Wu J, Yu X and Dai J 2022 Chinese Physics Letters 39 116301
- [34] Hao M and Guan P 2023 Chinese Physics B 32 098401
- [35] Li B, Yang Y, Fan Y, Zhu C, Liu S and Shi Z 2023 Chinese Physics Letters 40 097402
- [36] Zhang J, Chen G, Zhang C, Xu Y and Wang X 2025 Chinese Physics Letters
- [37] Zhuang L, Ye Q, Pan D and Li X Z 2020 Chinese Physics Letters 37 043101
- [38] Qiu R, Zeng Q, Wang H, Kang D, Yu X and Dai J 2023 Chinese Physics Letters 40 116301
- [39] Chang X, Kang D, Chen B and Dai J 2025 Chinese Physics Letters
- [40] Gao T, Zeng Q, Chen B, Kang D and Dai J 2024 Acta Metall. Sinica 60 1439
- [41] Zeng Q, Chen B, Kang D and Dai J 2023 Acta Phys. Sin. 72 187102-1 (in Chinese)
- [42] Liu L, Shi J, Song D and Miao C 2025 Phys. Chem. Chem. Phys. 27 11684
- [43] D'Souza J X, Hu S X, Mihaylov D I, Karasiev V V, Goncharov V N and Zhang S 2025 Phys. Plasma 32 042701

- [44] Pan S, Shi J, Liang Z, Liu C, Wang J, Wang Y, Wang H T, Xing D and Sun J 2024 Phys. Rev. B 110 224101
- [45] Zeng X, Xiao S, Chen Y, Li X, Wang K, Deng H, Zhu W and Hu W 2025 PHYSICA B 715 417499
- [46] Hou E, Wang X and Wang H https://www.aissquare.com/models/detail?pageType=models&name=DP-PbSn&id=355 [2023-09]
- [47] Mo P, Li C, Zhao D, Zhang Y, Shi M, Li J and Liu J 2022 Npj Comput. Mater. 8 107
- [48] Wang H, Zhang L, Han J and E W 2018 Comput. Phys. Commun. 228 178
- [49] Chen M, Guo G and He L 2010 J. Phys. Condens. Matter 22 445501
- [50] Li P, Liu X, Chen M, Lin P, Ren X, Lin L, Yang C and He L 2016 Comput. Mater. Sci 112 503
- [51] Perdew J P, Burke K and Ernzerhof M 1996 Phys. Rev. Lett. 77 3865
- [52] Hamann D R 2013 Phys. Rev. B 88 085117
- [53] van Setten M, Giantomassi M, Bousquet E, Verstraete M, Hamann D, Gonze X and Rignanese G M 2018 Comput. Phys. Commun. 226 39
- [54] Tantardini C, Iliaš M, Giantomassi M, Kvashnin A G, Pershina V and Gonze X 2024 Comput. Phys. Commun. 295 109002
- [55] Marsh S P 1980 LASL Shock Hugoniot Data vol 5 (Berkeley: University of California Press)
- [56] Li W, Hahn E N, Yao X, Germann T C and Zhang X 2019 Acta Mater. 167 51
- [57] Plimpton S 1995 J. Comput. Phys. 117 1
- [58] Larsen P M, Schmidt S and Schi
 øtz J 2016 Model. Simul. Mater. Sci. Eng. 24 055007
- [59] Stukowski A 2009 Model. Simul. Mater. Sci. Eng. 18 015012
- [60] Alippi P, Marcus P and Scheffler M 1997 Phys. Rev. Lett. 78 3892
- [61] Waitz T and Karnthaler H 1997 Acta Mater. 45 837
- [62] Pitsch W 1959 Philos. Mag. 4 577